Compression Stress-Induced Internal Magnetic Field in Bulky TiO₂ Photoanodes for Enhancing Charge-Carrier Dynamics

Binbin Wu, Yanhong Lyu, Wei Chen, Jianyun Zheng,* Huaijuan Zhou, Roland De Marco, Nataliya Tsud, Kevin C. Prince, Viacheslav Kalinovych, Bernt Johannessen, San Ping Jiang, and Shuangyin Wang

ACCESS | 📊 Metrics & More | 📖 Article Recommendations | 🆂🅸 Supporting Information

ABSTRACT: Enhancing charge-carrier dynamics is imperative to achieve efficient photoelectrodes for practical photoelectrochemical devices. However, a convincing explanation and answer for the important question which has thus far been absent relates to the precise mechanism of charge-carrier generation by solar light in photoelectrodes. Herein, to exclude the interference of complex multi-components and nanostructuring, we fabricate bulky TiO₂ photoanodes through physical vapor deposition. Integrating photoelectrochemical measurements and in situ characterizations, the photoinduced holes and electrons are transiently stored and promptly transported around the oxygen-bridge bonds and 5-coordinated Ti atoms to form polarons on the boundaries of TiO₂ grains, respectively. Most importantly, we also find that compressive stress-induced internal magnetic field can drastically enhance the charge-carrier dynamics for the TiO₂ photoanode, including directional separation and transport of charge carriers and an increase of surface polarons. As a result, bulky TiO₂ photoanode with high compressive stress displays a high charge-separation efficiency and an excellent charge-injection efficiency, leading to 2 orders of magnitude higher photocurrent than that produced by a classic TiO₂ photoanode. This work not only provides a fundamental understanding of the charge-carrier dynamics of the photoelectrodes but also provides a new paradigm for designing efficient photoelectrodes and controlling the dynamics of charge carriers.

KEYWORDS: enhanced charge separation and transfer, bulky TiO₂ photoanode, compressive stress-induced ferromagnetism, electromagnetic interaction
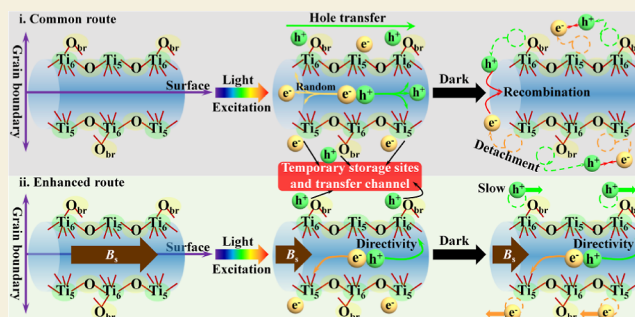
Conversion of solar energy into chemical fuels is a promising route for simultaneous storage of solar energy and the synthesis of value-added chemicals.[1−3] Photoelectrochemical (PEC) technology is one of the most effective approaches to directly realize solar energy conversion by combining the light absorber and the catalyst into a fully integrated system.[4,5] Currently, PEC tandem devices with designable photoanodes and photocathodes can sustain various bias-free redox reactions, including water splitting, CO₂ reduction reaction, and N₂ reduction reaction.[6,7] A series of inorganic semiconductor-based photoelectrodes have been studied and developed in the recent decade, which can be classified by metal oxides, metal chalcogenides, III−V compounds, and IV group.[8] Nanostructured photoelectrodes (e.g., nanotubes, nanowires) with good light harvesting and a short charge-migration distance have been widely studied and developed over the past 3 decades. But there is currently no practical nanostructured photoelectrode in the large-scale PEC device due to easy damage, ready corrosion, and poor adhesion strength between nanostructured materials and the conductive substrate. On the contrary, bulky photoelectrodes are durable

but ineffective, especially low charge separation and transport, limiting their PEC application.[9] This is because the driving force of the separation and transport processes solely is the weak electric field of photoelectrode—electrolyte interface originating from the surface space charge layer associated with the band bending. The width of the space charge layer is less than 100 nm, which cannot completely influence the separation and transport processes in the bulky photoelectrodes with the thickness of several micrometers.[10]

For a given semiconductor with the same surface morphology, band structure, and film thickness (>1000 nm),[11] the charge-carrier dynamics including the separation, transport, and injection of charge carriers is the crucial factor in determining its PEC performance. Accordingly, a systematic
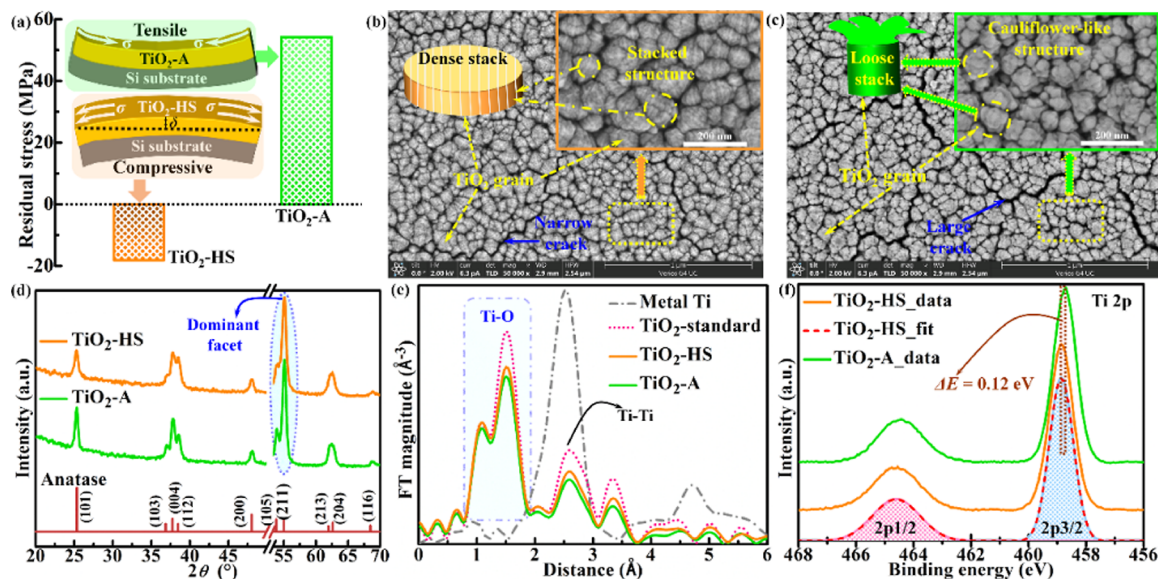
Figure 1. Characterization of stress, structure, and composition for bulky TiO$_2$ photoanodes. (a) Residual stress of TiO$_2$-HS and TiO$_2$-A. The sketches are the schematic diagrams of compressive stress and tensile stress for the films. (b,c) FESEM images with different magnifications for the top view of TiO$_2$-HS (b) and TiO$_2$-A (c). The inset is the schematic diagram of each sample in the corresponding figure. (d) GIXRD patterns of TiO$_2$-HS (orange) and TiO$_2$-A (green). The standard XRD card for anatase TiO$_2$ (red) is shown at the bottom (JCPDS, no. 04-0477). (e) Fourier transform of the measured EXAFS spectra of TiO$_2$-HS (orange solid line), TiO$_2$-A (green solid line), standard anatase TiO$_2$ (red dotted line), and metal Ti (gray dash-dotted line). (f) Ti 2p spectra of TiO$_2$-HS (orange) and TiO$_2$-A (green) from XPS measurements. Taking TiO$_2$-HS as an example, Ti 2p spectrum of TiO$_2$-HS is deconvoluted into 2p$_{2/3}$ (blue) and 2p$_{1/2}$ (pink) peaks.

and rigorous analysis and study of intrinsic charge-carrier dynamics must be carried out in an effort to understand the fundamental mechanism providing options for the maximization of PEC reaction efficiency.[12] Taking metal oxide semiconductors as a typical photoelectrode material,[13] the prevailing view is that the semiconductors are irradiated by solar light to yield the photoexcited hole−electron pairs, also known as excitons.[14] For most metal oxide semiconductors, the photoexcited holes and electrons are prone to couple with the lattices (electron/hole−phonon coupling) to form small polarons in the bulk due to the strong ionic character of metal oxides.[15] Subsequently, charge transport in the semiconductors can occur through thermal activation with either polaron hopping[16] or thermal excitation from defect trap sites.[17] However, although some coupled charge carriers can arrive at the solid/liquid interfaces and contribute to the PEC reactions with a certain probability, there are multiple bulk and surface recombination processes that lead to loss of many of the charge carriers (return to the ground state),[18] attributed to disordered motion and neighboring polaron sites for the photogenerated electrons and holes. In addition, the extracted charge carriers (like holes) interact with surface defect sites (like oxygen-bridge bonds) more easily, leading to the formation of reaction active sites (like oxygen vacancies) and the acceleration of reaction kinetics.[19]

These pioneering and important investigations offer constructive guidance for intrinsic charge-carrier dynamics, while leaving aspects of the charge-carrier dynamics unclear. For instance, semiconductor photoelectrodes are composed of small crystalline grains with grain boundaries and unsaturated bonds, which would interfere with and complicate the charge-carrier dynamics. Some critical questions remain unanswered. For example, what are the roles and intermediate forms of these unsaturated bonds during PEC reaction, and how does the bulk and grain boundary bridge? Furthermore, what are the

intrinsic coupling sites associated with photogenerated holes and electrons in the formation of the polarons, if formed without the influence of inducing intentional defect sites, such as doping with foreign atoms? Meanwhile, what is the effect of the spatial segregation of different polarons in the reduction of the recombination of charge carriers for bulky photoelectrodes? Finally, what is the fundamental contribution of charge-carrier separation/transport and injection to the PEC performance for a photoelectrode? These fundamental questions must be addressed.

Herein, the most studied and widely applied titanium dioxide (TiO$_2$) material, mainly owing to the natural abundance, nontoxicity, and the resistance to photocorrosion, was chosen as a model binary oxide photoanode to decipher the enhanced charge-carrier dynamics.[20−22] Well-defined flat and thick TiO$_2$ photoanodes (over 1 μm thickness) with and without compression stress were prepared by physical vapor deposition and annealing treatment. According to the aforementioned requirements, we combined the phenomena of PEC reactions and the results of operando measurements to reveal the formation of polarons, the transport of charge carriers, and the surface active sites for TiO$_2$ photoanodes. Inspired by the correlation between the strain/stress and the magnetic structure of the film,[23,24] we also observed the enhanced charge-carrier dynamics for TiO$_2$ photoanode by compressive stress-induced ferromagnetism for the first time, achieving an increase of over 2 orders of magnitude, which is an exciting development with this new technology platform.

■ METHODS

The TiO$_2$-based photoanodes with and without compression stress were fabricated by magnetron sputtering technology and annealed treatment. The details for the synthesis of the TiO$_2$-based photoanodes are shown in the Experimental Methods of the Supporting Information. In addition, a detailed statement of the ex
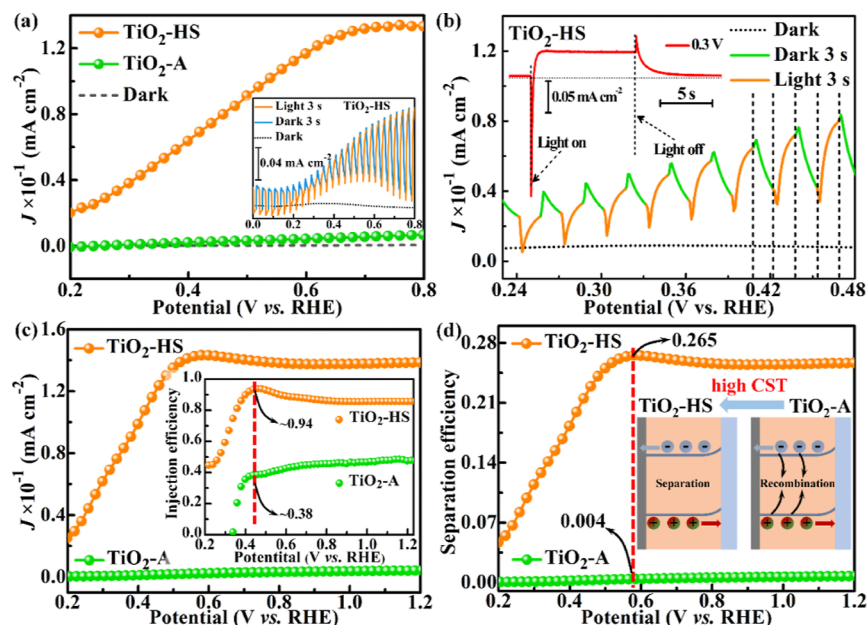
Figure 2. PEC performance characteristics for the bulky TiO$_2$ photoanodes. (a) J-potential plots of TiO$_2$-HS and TiO$_2$-A measured in 1 M KOH under AM 1.5 G simulated sunlight (100 mW cm^{-2}) and in the dark (black dotted lines) with a scan rate of 5 mV s^{-1}. The inset is the corresponding chopped J-potential curve of TiO$_2$-HS (light on/off cycles: 3 s). (b) Chopped curve of TiO$_2$-HS from 0.225 to 0.495 V vs RHE. The inset is the J-time plots of TiO$_2$-HS at the potential of 0.3 V vs RHE under light irradiation (light on: 10 s) and in the dark. (c) J-potential curves of TiO$_2$-HS and TiO$_2$-A for PEC sulfite oxidation measured in 1.0 M NaOH with 0.05 M Na$_2$SO$_3$ under 1 sun illumination. The inset is the charge-injection efficiency calculated from (c,a). (d) Charge-separation efficiency of the bulky TiO$_2$ photoanodes calculated by the ratio of J values of sulfite oxidation to J_{abs}. The inset is the schematic of charge separation and recombination for TiO$_2$-HS and TiO$_2$-A in the bulk, respectively.

situ and in situ characterization and PEC measurements is described in the Supporting Information.

RESULTS AND DISCUSSION

As reported in our previous work,[25] the micron-sized TiO$_2$ films with high compressive stress (TiO$_2$-HS) were grown on titanium-coated p-Si substrates by magnetron sputtering technology. After film deposition, annealing treatment at 500 °C for 60 min was implemented to release the residual compressive stress to obtain normal TiO$_2$ films (TiO$_2$-A) with tensile stress, which is commonly used in the study of TiO$_2$ photoanodes.[26−28] In addition to the optimized deposition condition, a series of TiO$_2$ films with different compressive stresses and structures were also prepared. The formation of residual internal stress for the TiO$_2$ films prepared by magnetron sputtering is schematically demonstrated in Figure S1. The residual internal stress of the photoanodes in Figures 1a and S2 indicates that the internal stress value of TiO$_2$-HS was −18.2 MPa, confirming the residual compressive stress. As a rule of thumb, the formation of compression stress is closely related to the highly dense microstructure of the film. After annealing, the internal stress of TiO$_2$-A was completely transformed into the tensile stress of 54.3 MPa, implying the relaxation of compressive stress and grain boundaries.

Field emission scanning electron microscopy (FESEM) images were used to outline the architecture of the thick TiO$_2$ photoanodes (Figures 1b,c, S3, and S4). The TiO$_2$-HS and TiO$_2$-A photoanodes composed of columnar crystal grains had the same film thickness over 1.2 μm, meaning that the films can be considered for the bulky TiO$_2$ photoanodes. Instead of a loose stack of grains for TiO$_2$-A (Figure 1c), the crystal grains of TiO$_2$-HS were dense (Figure 1b), in line with the results of internal stress. High-resolution transmission electron microscopy (TEM) images (Figure S5) indicated that TiO$_2$-

HS possessed a dense columnar structure with a narrower (101) plane of anatase TiO$_2$ corresponding to the lattice spacing of 0.344 nm. Atomic force microscopy images illustrate that both TiO$_2$-HS and TiO$_2$-A had flat surfaces with a root-mean-square roughness of 9.7 and 9.2 nm, respectively (Figure S6). As shown in Figure S7, TiO$_2$-HS and TiO$_2$-A have a very low specific surface area (A_s) with few nanopores (pore diameter = ∼5 nm) on the surface, in agreement with the microstructure and morphology of the samples via FESEM and TEM images. The crystalline structure of the photoanodes was characterized by grazing incidence X-ray diffraction (GIXRD) patterns (Figures 1d and S8). An ignorable difference of diffraction peaks was observed in TiO$_2$-HS and TiO$_2$-A, shielding the interference of high-energy (211) facet. In addition to the similar crystal structure, some diffraction peaks [such as (105)] of TiO$_2$-HS showed a little shift toward a higher angle than those of TiO$_2$-A (see Figure S8b), indicating the presence of lattice contraction by compressive stress. Ti K-edge X-ray absorption spectroscopy (XAS) spectra of the photoanodes containing X-ray absorption near-edge structure (see Figure S9) and extended X-ray absorption fine structure (EXAFS, see Figure 1e) reveal that TiO$_2$-HS and TiO$_2$-A possessed an anatase structure, albeit with a lower coordination number, due to the two-dimensional nature of the structure, in comparison to the standard anatase TiO$_2$ bulk.

The full survey spectrum from TiO$_2$-HS acquired X-ray photoelectron spectroscopy (XPS) presented only the characteristic peaks of Ti 2p, O 1s, and C 1s (Figure S10a). The dominant peak of Ti 2p$_{3/2}$ for TiO$_2$-HS was centered at 458.86 eV (see Figure 1f) corresponding to Ti^{4+},[29] which is higher than that for TiO$_2$-A (458.74 eV), demonstrating a slight electronic reconstruction in the coordination environment of Ti cations. A similar trend was also observed in the O 1s spectra of TiO$_2$-HS and TiO$_2$-A (Figure S10b). Under high

compressive stress, the strong d−d Coulomb interaction between Ti atoms results in a stronger Jahn−Teller distortion of the Ti−O bonds,[30] leading to the formation of the dipoles. The charge transfer between Ti and coordinated O triggered by a strong spin−orbit interaction can induce a positive shift of the Ti $2p_{3/2}$ core level. According to our optical measurements and an indirect allowed transition of TiO_2, both TiO_2-HS and TiO_2-A showed the band gap of ~3.2 eV (see Figure S11a,b). Additionally, by integrating the absorbance across AM 1.5G solar spectrum (Figure S11c,d), the photocurrent densities at 100% internal quantum efficiency (J_{abs}) for TiO_2-HS and TiO_2-A were calculated to be ~0.54 and 0.56 mA·cm^{-2}, respectively. In other words, apart from the internal stress and electronic structure, TiO_2-HS and TiO_2-A show nearly the same composition, crystalline structure, surface morphology, film thickness, and band gap, indicating the same capabilities of light harvesting.

It is generally known that annealing can improve the crystallinity of TiO_2 photoanodes and enhance their PEC oxygen evolution reaction (OER) performance. For example, amorphous TiO_2 after annealing has a better PEC OER performance than amorphous TiO_2 (Figure S12a,b). Surprisingly, from photocurrent density (J)−potential plots (Figure 2a), TiO_2-HS showed a higher saturated J of ~0.13 mA·cm^{-2} and a lower onset potential (~0.6 V vs RHE) than TiO_2-A, meaning a better PEC OER performance. In fact, compared to the reported data on recent work of TiO_2-based film (see Table S2), the TiO_2 films with high compressive stress achieve a comparable PEC performance. Based on both the composition and structure characterizations above, it indicates that the unique compression stress and induced electronic structure can significantly influence the PEC behaviors of TiO_2 photoanodes. In comparison to TiO_2-HS, the thinner TiO_2 photoanodes with lower compression stress displayed a worse PEC OER performance (Figure S12c,d) but a performance superior to the PEC results of TiO_2-A. Meanwhile, to exclude the disturbance of film thickness, the J-potential plots of TiO_2 photoanodes with the same film thickness and different stresses also showed the different PEC OER behaviors (see Figure S13). These results can provide further evidence for the positive correlation between the compression stress and PEC OER performance. The chronoamperometry measurements and gas collection were carried out to solidify the occurrence of PEC OER via TiO_2-based photoanodes, as shown in Figure S14.

The chopped J-potential curves for the bulky TiO_2 photoanodes were acquired to study the transient response of J and assess the PEC intrinsic behaviors. Normally, the chopped J-potential curves of normal TiO_2 photoanodes are basically identical with their J-potential curves under illumination and in the dark, as demonstrated by the PEC behaviors of TiO_2-A and amorphous TiO_2 (Figures S12b and S15b,e). However, TiO_2-HS with high compression stress showed an unusual chopped J-potential curve via 3 s turn-on and 3 s turn-off (the inset of Figure 2a), in which the J in the dark was substantially higher than the base current of TiO_2-HS in the dark (see the dashed black line of Figure 2a) and a bump was observed in the curve, ranging from 0.2 to 0.8 V versus RHE. Moreover, when the potentials were fixed at certain values, the chopped J-time curves of TiO_2-HS (Figures 2b and S16) provided some interesting phenomena. First, in the split second of light turn-on, a sharp and short reduction current with less than 1 s was recorded at the various potentials, like

0.3 V versus RHE (Figure 2b). There is no observation of such a reduction current in the normal TiO_2 photoanodes, such as TiO_2-A (Figure S15e). Correspondingly, a distinct oxidation current was observed as the light turned off. The oxidation current exhibited two features: (1) a higher onset current density than the J at stable operation and (2) a long decay time for over 11 s (Figure S16d). On the basis of the long decay oxidation current, we can hypothesize that the appearance of the bump in the chopped J-potential curve of TiO_2-HS is strongly coupled between the chopped time in the dark and the decay time of oxidation current. The chopped J-potential curves for TiO_2-HS with different chopped times in the dark (Figure S17) were investigated to verify the hypothesis. As hypothesized, the size of the bump in the chopped J-potential curves was controlled by varying the chopped time in the dark (Figure S17g).

The PEC reaction on the photoelectrode predominantly involves three synergistic processes: light absorption, charge separation, and charge injection.[31] The J of the reaction is generalized as

$$J = J_{abs} \times \eta_{sep} \times \eta_{inj} \tag{1}$$

where J_{abs}, η_{sep}, and η_{inj} are the J at 100% internal quantum efficiency, the efficiency of the separation and transport of photogenerated charge carriers in the bulk, and the efficiency of surface-reaching charges that reacted with the electrolytes, respectively. To quantify the η_{inj} and η_{sep}, J-potential curves of PEC sulfite oxidation were measured in 1.0 M NaOH with 0.05 M Na_2SO_3 hole scavenger under AM 1.5G illumination (Figure 2c). PEC sulfite oxidation was regarded as $\eta_{inj,sul}$ of 100% to assess the charge dynamics of the bulky photoanodes owing to the thermodynamically and kinetically more facile reaction process.[32] For the same photoanode, the $\eta_{inj,OER}$ of OER can be obtained by the following relationship

$$\eta_{inj,OER} = \frac{J_{OER}}{J_{sul}} \tag{2}$$

where J_{OER} and J_{sul} are the J for OER and sulfite oxidation, respectively. In the inset of Figure 2c, the higher value of $\eta_{inj,OER}$ of ~94% was achieved with TiO_2-HS at 0.46 V versus RHE, which is over 2 times higher than the result for TiO_2-A (~38%). Furthermore, the electrochemical surface areas (ECSAs) of TiO_2-HS and TiO_2-A measured by electrochemical double-layer capacitance (C_{dl}) were ~25 and 8 μF· cm^{-2}, respectively (see Figure S18), in almost agreement with the difference of $\eta_{inj,OER}$ between TiO_2-HS and TiO_2-A. These results can associate with the increase of surface active sites via high compression stress. Most importantly, the η_{sep} of TiO_2-HS and TiO_2-A was obtained by the equation

$$\eta_{sep} = \frac{J_{sul}}{J_{abs}} \tag{3}$$

where J_{abs} of TiO_2-HS and TiO_2-A is ~0.54 and 0.56 mA·cm^{-2}, respectively. In Figure 2d, the η_{sep} of 26.5% in TiO_2-HS was achieved at 0.58 V versus RHE, which is ~66 times higher than that of TiO_2-A (0.4%). This expected result can suggest that the thick TiO_2 photoanodes with high compression stress have an internal field in the bulk to drive the separation and transfer of charges. Meanwhile, the data of electrochemical impedance spectroscopy (see Figure S19a) and intensity-modulated photocurrent spectra (see Figure S19b) demonstrated that TiO_2-HS possesses lower charge-transfer resistance and higher
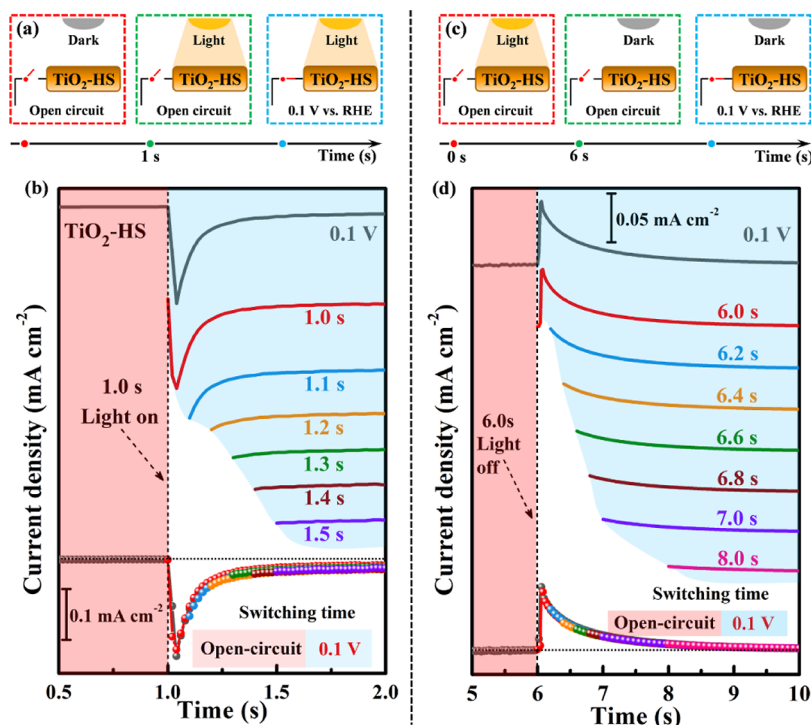
Figure 3. Distinguishing the electrical and optical characteristics for TiO_2-HS photoanodes. (a,c) Schematic diagrams of photoelectric tests for distinguishing the photoexcited and electrical characteristics for TiO_2-HS photoanodes at the moment of light on (a) or light off (c). (b) Current density−time plots of TiO_2-HS at 0.1 V while connecting the circuit at different times (light on at 1 s). (d) Current density−time plots of TiO_2-HS at 0.1 V while connecting the circuit at different times (light off at 6 s).
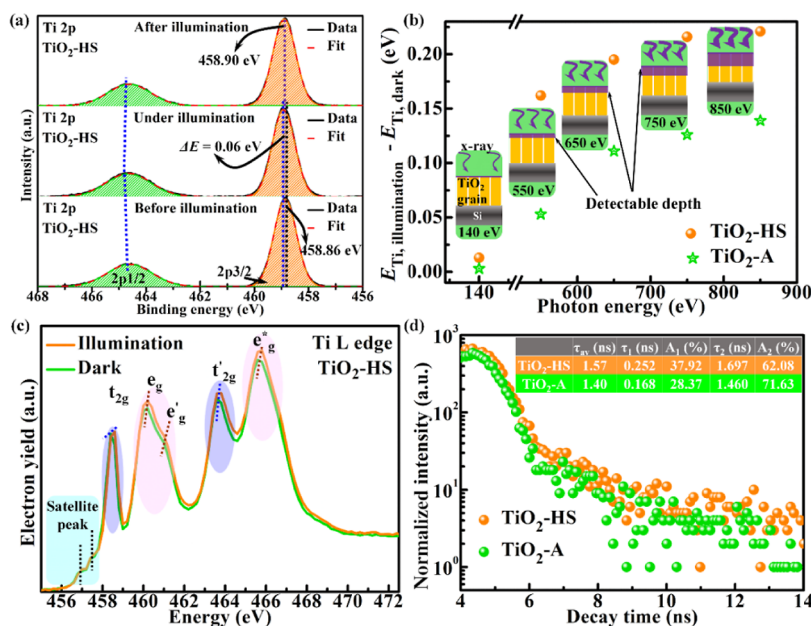

Figure 4. Various operando physical/chemical measurements on the bulky TiO_2 photoanodes. (a) Ti 2p spectra of XPS for TiO_2-HS before, during, and after illumination. (b) Difference between Ti dominant peak positions with and without illumination as a function of photon energy for TiO_2-HS and TiO_2-A measured with SR-XPS. The illustrations display the increase of X-ray detectable depth with increasing photon energy. (c) Electron-yield Ti L-edge NEXAFS of TiO_2-HS under illumination (orange line) and in the dark (green line). (d) TRPL decay curves for TiO_2-HS and TiO_2-A at room temperature. The inserted table shows the lifetime of photogenerated charge carriers.

charge-carrier concentration under illumination than TiO_2-A, supporting the results of their η_{sep}. Consequently, the separation and transfer of photogenerated charges in the bulk are the predominant factors to determine the PEC performance of the bulky TiO_2 photoanodes with high compression stress. The Mott−Schottky plots of the samples in Figure S20 were used to determine the flat band voltage. The x-intercepts of the Mott−Schottky plots plus kT/q (∼0.025 V, as described in eq S5) for TiO_2-HS and TiO_2-A give a flat band voltage of −0.6 and −0.55 V, respectively.

Obviously, the TiO_2 photoanodes with the compression stress behave very differently with respect to PEC properties as compared to the normal TiO_2 photoanodes, as shown in Figure 2b. Aiming to find the origin of this specific PEC behavior, the multiple-step simulated open-circuit PEC measurements (see Figure 3) were implemented to study the precise contribution of solar light and applied bias on the PEC performance of TiO_2 photoanodes. With respect to the reduction current at the instantaneous light turn-on, the PEC measurements (Figure 3a,b) were carried out according to the following three stages: (1) at 0−1 s, the PEC measurements were conducted under open-circuit conditions in the dark; (2) after 1 s, the light was turned on and TiO_2-HS was irradiated to yield the hole−electron pairs under open-circuit conditions; (3) finally, the circuit began to be connected at different times for the illuminated TiO_2-HS. It can be clearly seen that these J-time curves measured at different times of connecting the circuit almost overlapped in the J-time curve from normal PEC data (Figure 3b). Additionally, the oxidation current at the instantaneous light turn-off was investigated using similar three stages of PEC measurements, including the conditions of open circuit/light irradiation, open circuit/dark, and connecting the circuit/dark (Figure 3c,d). Similarly, the J-time plots of TiO_2-HS at different times for connecting the circuit completely coincided with the PEC plots for common measurement parameters (Figure 3d). It directly proves that for TiO_2-HS after turning light on/off, the sudden appearance of reduction/oxidation current and its decay process are solely related to the light, rather than the external potentials. As a result, the additional reduction/oxidation current after turning the light on/off is derived from the unique characteristics of TiO_2 photoanodes with the compression stress.

Operando XPS was carried out to understand the link between photoinduced charges and the electronic state of the photoanodes, and the results are shown in Figures 4a and S21. The high-resolution Ti 2p spectra of TiO_2-HS (Figure 4a) showed a recognizably positive energy shift (0.06 eV) during illumination relative to that before illumination (458.86 eV), indicating the stronger distortion at Ti−O bonds, consistent with the change of O 1s spectra during and before illumination (Figure S21). This result is ascribed to the transfer of photoinduced charges on the Ti and O sites, leading to the formation of active dipoles and the reconstruction of the electronic coordination environment during illumination. After removing the light, the Ti 2p peak of TiO_2-HS (458.90 eV) slightly shifts toward a lower binding energy but does not completely return to its original state before illumination (458.86 eV). The active dipoles for TiO_2-HS can be stabilized in the bulk under high vacuum conditions; that is, the charge carriers are stored temporarily.

Aiming to further explore the distribution of the electron reconstruction with different depths, we employed operando synchrotron radiation XPS (SR-XPS) to undertake depth profiling of the photoanodes using the tunable photon energy (E_{ph}) of the photon beam associated with the corresponding photoelectron kinetic energy (Figures 4b and S22−25).[33] As illustrated in Figure 4b, the sampling depth strongly depends on the photoelectron kinetic energy defined by E_{ph} when the energy is higher than ∼50 eV.[33] Deconvolution of the Ti 2p and O 1s spectra for TiO_2-HS and TiO_2-A (Figures S22−S25) from SR-XPS with different E_{ph} also exhibits a similar shift toward a higher binding energy under illumination related to that in the dark. The photoinduced distortion degree of Ti−O

bonds as well as the number of the formed dipoles was defined as the difference between the dominant peak positions of Ti 2p spectra under illumination and in the dark ($\Delta E = E_{Ti,illumination} - E_{Ti,dark}$). It is clearly seen in Figure 4b that the ΔE was 0.013, 0.162, 0.195, 0.216, and 0.221 eV corresponding to E_{ph} of 140, 550, 650, 750, and 850 eV, respectively, signifying fewer dipoles on the topmost surface (<1 nm) compared with the deeper surface region of the thick film. By correlating the SR-XPS results and FESEM images, we can speculate that the dipoles of TiO_2-HS are mainly concentrated on the grain boundaries, suggesting that the photoinduced charges would be easily trapped by the defects at grain boundaries, like 5-coordinated Ti atoms (Ti_5) and oxygen-bridge bonds (O_{br}). The altered trends of the distortion state of Ti−O bonds with the increase of E_{ph} were also observed in O 1s spectra (Figure S24) and TiO_2-A (Figures S23 and S25). In comparison to TiO_2-A, TiO_2-HS showed more efficient dipole productions throughout the whole bulky TiO_2 photoanode during illumination.

Near-edge X-ray absorption fine structure (NEXAFS) spectroscopic studies were carried out to identify the changes of the electronic and atomic structures itself from the light excitation. It is well known that the Ti L-edge NEXAFS of TiO_2 consists of two doublet peaks by the spin−orbit interaction of the Ti 2p core level with an electron transfer from the Ti $2p_{3/2}$ or $2p_{1/2}$ levels to the Ti 3d orbitals, resulting in the presence of t_{2g} and e_g orbitals in octahedral symmetry.[34] The Ti L-edge spectrum of TiO_2-HS (see Figure 4c) showed clearly the absorption features of anatase TiO_2 and no sign of Ti^{3+}.[35] When the illumination was introduced, the intensity of the t_{2g} and e_g peaks was slightly increased, which reflects the photogenerated electrons in the t_{2g}- and e_g-like orbitals. Meanwhile, the two doublet peaks of TiO_2-HS shifted to higher energy under illumination than in the dark, suggesting the redistribution and mixture of electron orbitals with the photogenerated electrons. Similar changes of the O K-edge NEXAFS spectra were also found in TiO_2-HS with and without irradiation (Figure S26). To further investigate the defect states in the bulk, we used electron paramagnetic resonance (EPR) spectroscopy to observe the TiO_2 photo-anodes with and without illumination at 130 K (Figure S27). No EPR signal of Ti^{3+}/oxygen vacancies was detected for the photoanodes in the dark and under illumination. Consequently, the properties of the bulky TiO_2 photoanodes are sensitive to the distortion of Ti−O bonds and the formation of active dipoles by the overlap of the excited-state electron orbitals, strongly correlating to the PEC performance, especially the charge separation and transport.

Photoluminescence (PL) emission spectroscopy is a powerful tool for judging the recombination of photogenerated charges of the photoelectrodes. Both TiO_2-HS and TiO_2-A had PL peaks centered at about 390 (almost being equal to 3.17 eV, see Figure S28), originating from the main emission of band-gap transitions and the recombination of charges. As compared to TiO_2-A, a marked fluorescence quenching was observed on TiO_2-HS, signifying the suppression of charge-carrier recombination. Time-resolved PL (TRPL) spectra can probe the charge lifetime of the photoanodes with the decay curves and kinetic parameters. As shown in Figure 4d, the charge lifetime of TiO_2-HS and TiO_2-A was 1.57 and 1.40 ns, respectively. However, such a slight increase of charge lifetime on TiO_2-HS in comparison to TiO_2-A hardly matches a substantial improvement in the process of charge separation
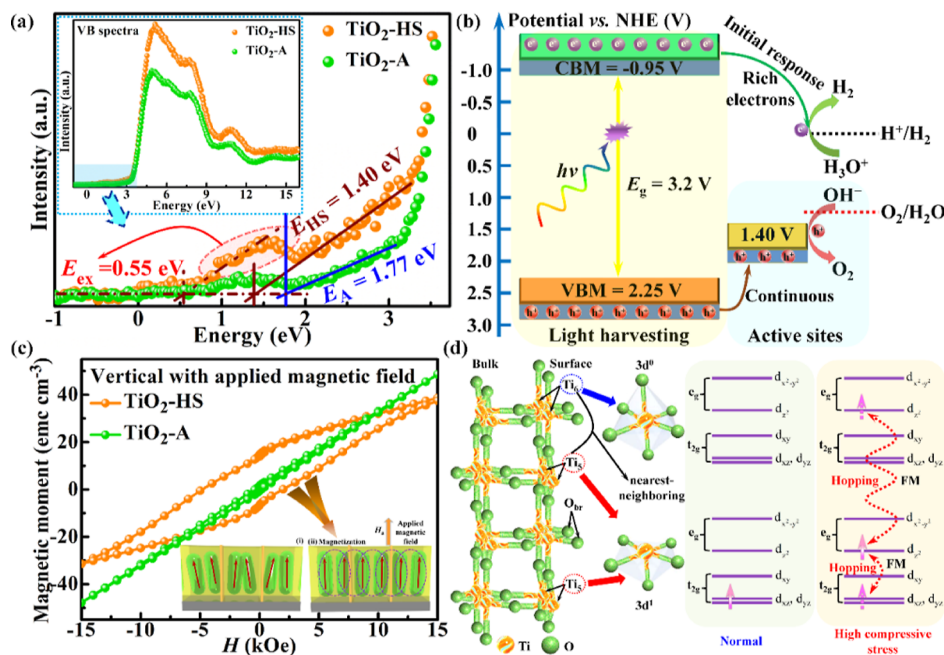
Figure 5. Contributions to the charge-carrier dynamics of TiO$_2$ photoanodes. (a) SR-XPS VB spectra from −1 to 3.5 eV for TiO$_2$-HS and TiO$_2$-A with E_{ph} of 140 eV. The inset shows SR-XPS VB spectrum from −1 to 16 eV. (b) Proposed schematic of the band structure for TiO$_2$-HS. (c) Room-temperature hysteresis curves of TiO$_2$-HS and TiO$_2$-A with applied magnetic field perpendicular to the photoanode surface. The schematic diagram illustrates the production of room-temperature ferromagnetism. (d) Origin of the ferromagnetic state for TiO$_2$-HS by stress-induced indirect exchange interactions between Ti ions.

and transport. One possible reason would be that the photogenerated charges of the bulky TiO$_2$ photoanodes with high compression stress are quickly transferred and stored as efficient dipoles to enhance PEC performance, which is in line with the observations made in this study.

Valence band (VB) analysis of TiO$_2$ photoanodes (Figure 5a) was performed by SR-XPS to clarify the band structure of the surface. The TiO$_2$-A displayed a low intensity of the density of states (DOS) with the edge of the VB maximum at 1.77 eV and shows characteristics identical to the classical VB characteristics of TiO$_2$. By contrast, a pronounced shift of the VB maximum (1.40 eV) toward a lower energy was found on TiO$_2$-HS. Additionally, TiO$_2$-HS also had a bump near the Fermi level with an edge of 0.55 eV, assigned to the presence of active dipoles via the compression stress-induced interaction of electron orbitals. As suggested by Pan et al.,[36] the VB maximum values in electron volts can be converted to electrochemical energy potentials in volts to reconstruct the band structure of TiO$_2$ photoanodes. The scheme of the band structure for TiO$_2$-HS in Figure 5b shows clearly the transfer of photoexcited holes. The band gap of TiO$_2$-HS is 3.07 V with the VB maximum of 2.25 V and the CB minimum of −0.82 V, which satisfies the requirements of PEC overall water splitting. Concurrently, the additional active dipoles at 1.40 V can facilitate the transfer of holes through the VB for participation in PEC OER.

Electricity and magnetism are separate yet interconnected phenomena associated with moving electric charges, and a magnetic field can change the movement of electric charges to produce an electric current. To further illuminate the real origins of the enhanced charge-carrier dynamics, the room-temperature ferromagnetism of the bulky TiO$_2$ photoanodes was studied by applying a magnetic field perpendicular to the surface of the photoanode (Figure 5c). TiO$_2$-A exhibited a

visible paramagnetic behavior, while TiO$_2$-HS demonstrated clear ferromagnetism with an apparent ferromagnetic saturation moment (M_s) of ~38 emu cm^{-3} and an intrinsic coercivity (H_c) of ~2 kOe. When a parallel magnetic field was applied at the surface, a slight diamagnetism was found on TiO$_2$-HS (Figure S29). The magnetic anisotropy of TiO$_2$-HS can be ascribed to the motion of non-180° magnetic domain walls driven by compressive stress toward the perpendicular direction to form the long-range magnetic moments under external magnetic fields (see the inset of Figure 5c).[23] In addition, to distinguish the annealing conditions of TiO$_2$-A (500 °C, 60 min), the annealing conditions were set as 400 °C, 30 min to obtain the TiO$_2$ film with low compressive stress. The decrease of compressive stress can result in the demagnetization of TiO$_2$ film (Figure S30) and the corresponding decrease of photocurrent density (Figure S13). Thus, the PEC performance of TiO$_2$ film is proportional to its ferromagnetic behavior. However, the demagnetization of TiO$_2$ films by annealing is irreversible and difficult to magnetize again by other methods. This is because the magnetic domain hardly overlaps the adjacent TiO$_2$ grains with loose structures after annealing, leading to the lack of a net alignment of polaron spins (see Figure S31).

The mechanism that brings about the ferromagnetic interaction of TiO$_2$-HS is schematically depicted in Figure 5d. For a perfect TiO$_2$ crystal grain, each Ti atom in an octahedral ligand field should be fully coordinated with six O atoms (labeled as Ti$_6$) and split into high e$_g$ and low t$_{2g}$ orbitals (see Figure 5d). In fact, Ti atoms on the surface of the real crystal grain possess unpaired 3d orbitals with a single electron (labeled as Ti$_5$). Usually, each t$_{2g}$ orbital in Ti$_5$ is occupied by the single electron with a single spin, making the unfilled 3d-shell act as a spin-dependent gate to adjust charge transfer. One proposed route is that the electronic hopping between
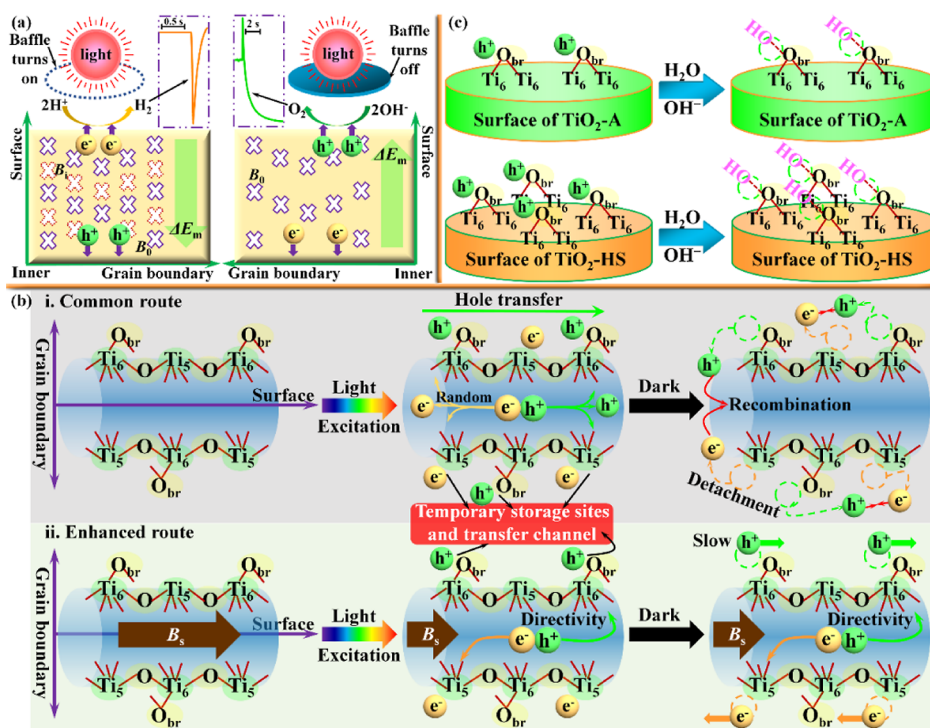
Figure 6. Intrinsic and enhanced mechanisms of charge-carrier dynamics for TiO$_2$ photoanodes. (a) Schematic diagrams of magnetically induced voltages corresponding to PEC reactions when the light turns on (left) and turns off (right). (b) Separation and transfer of photogenerated electron−hole pairs for TiO$_2$ photoanodes: (i) common route and (ii) enhanced route. (c) Schematic diagrams of the surface catalytic effect of TiO$_2$ photoanodes for PEC OER.

half-filled t$_{2g}$ orbital and unfilled e$_g$ orbital results in a ferromagnetic behavior (Figure 5d).[36] On the other hand, the indirect exchange coupling, which is an excited electron from the 2p orbital into a vacant 3d orbital of Ti6 directly interacting with the 3d orbital of the nearest-neighboring Ti$_5$, gives rise to a ferromagnetic interaction between the nearest-neighboring Ti$_6$ and Ti$_5$ (Figure 5d).[37] In these cases, we can imagine that the electronic hopping and interaction are impelled to form the well-aligned dipole moments when the compressive stress is applied, contributing to a magnetic structure conversion and spin reconfiguration.

Integrating the PEC OER performance, operando physical and chemical characterization, and the exchange interaction of magnetic and electric fields, the compression stress-induced internal magnetic field can be the dominating factor for enhancing the charge-carrier dynamics of the bulky TiO$_2$ photoanodes. Meanwhile, some important appearance factors such as surface morphology, film thickness, and ECSA can reflect and tune the residual stress of TiO$_2$ photoanodes for improving the PEC behaviors. However, in this work, the influence of oxygen vacancies, crystallinity, and light absorption on the PEC performance can be safely ruled out as testified in Figures S8, S11, and S27. Consequently, the mechanisms of enhanced charge dynamics for the bulky TiO$_2$ photoanodes are proposed in Figure 6, including the separation, storage, transfer, injection, and recombination of the photogenerated charges. When the anisotropic magnetism induced by compressive stress is taken into account, each crystal grain in the bulky TiO$_2$ photoanodes can be passed through magnetic induction lines from adjacent crystal grains. For the photoanode, the holes continuously move to the surface under stable illumination due to the band bending at the solid/liquid interface. However, according to Lenz's law, in

an instant of switching on the light, the original magnetic field can yield an induced electromotive force to impede the motion of holes and drive the electrons from the subsurface into the solid/liquid interface so that they may participate in the hydrogen evolution reaction (HER). The time of HER is short (less than 0.5 s), resonant with the dynamics of the induced electromotive force (see the left-hand side of the scheme in Figure 6a). By contrast, when the light is switched off, an opposite induced electromotive force from the original magnetic field can facilitate the transfer of holes, which corresponds to an increase in the transient current as depicted in the right-hand side of the scheme in Figure 6a. It is important to note that the decay time of current in the dark is over 11 s, which is prolonged compared to the effect of induced electromotive force. Accordingly, this long decay time is due to the combined action of the induced electromotive force, prolonged-release holes/electrons, and non-recombination charge transfer.

Taking a common TiO$_2$ crystal grain as an example, the O$_{br}$ and Ti$_5$ sites are uniformly surrounded by the boundaries of the grain to capture the holes and electrons, respectively. Upon illumination, TiO$_2$ absorbs the photons and produces electrons and holes. The excited electrons and holes can randomly move in any direction following Brownian movement. This process gives rise to the recombination of a number of holes and electrons, and the residual charge carriers migrate to the uncoordinated sites of the boundaries to form the active dipoles [Figure 6b(i)]. The dipoles play the roles of temporary storage sites and transfer channels of charge carriers. Nevertheless, the positive and negative dipoles are contiguously dispersed in the boundaries, leading to the occurrence of charge recombination when the holes/electrons transfer in the bulk/surface. Back to the dark condition, the holes and

electrons are released by the dispersed positive and negative dipoles, which sequentially and quickly recombine. Normally, no decay current can be found in this scenario. However, if the TiO$_2$ grain has a ferromagnetism perpendicular to the surface, an intrinsic magnetic field is established with the grain. From the perspective of the Lorentz force law, the photogenerated holes and electrons possessing different charges in the magnetic field travel in opposite directions [Figure 6b(ii)]. The holes and electrons directionally arrive at the opposite boundaries to create the completely separated positive and negative dipoles, respectively. Under irradiation, the holes and electrons are smoothly transported from the bulk to the surfaces of the TiO$_2$ photoanode and counter electrode to split water into oxygen and hydrogen, respectively. Returning to the dark, an obvious persistent current is generated by the released holes and electrons due to free charge recombination [Figure 6b(ii)]. As a result, the directional motion and the separated positive and negative dipoles can tremendously increase the efficiency of charge separation and transport. Considering the distortion of Ti−O induced by compressive stress, the surface of TiO$_2$-HS yields more active dipoles that adsorb more dissociated H$_2$O molecules, in comparison to that of TiO$_2$-A. In Figure 6c, these active dipoles embodying the injection of holes facilitate the reaction in the solid/liquid interface.

CONCLUSIONS

In summary, this study has provided unequivocal evidence of the enhanced mechanism of charge separation and transfer for the bulky TiO$_2$ photoanodes, which is critical to realizing a highly efficient PEC oxidation reaction. Our work demonstrates that the dipoles formed at the grain boundaries via photoexcited charge carriers and the uncoordinated sites play an important role in charge separation, transport, and storage. Under compression-stress-induced ferromagnetic field, the bulky TiO$_2$ photoanodes exhibit a significant increase in charge separation and transfer in the bulk (over 60 times) and a slight increase in charge injection on the surface (∼2 times), in comparison to the normal TiO$_2$ photoanodes. We anticipate that the insights reported here will draw more attention to the necessity to further improve the charge separation and transfer and achieve better PEC performance by novel routes.

ASSOCIATED CONTENT

Supporting Information

The Supporting Information is available free of charge at https://pubs.acs.org/doi/10.1021/jacsau.2c00690.

Preparation, physicochemical characterization, performance testing, and operando analysis of the samples (PDF)

AUTHOR INFORMATION

Corresponding Author

Jianyun Zheng − *State Key Laboratory of Chem/Bio-Sensing and Chemometrics, College of Chemistry and Chemical Engineering, Hunan University, Changsha 410082 Hunan, China;* ⊙ orcid.org/0000-0002-2262-7694; Email: jyzheng@hnu.edu.cn

Authors

Binbin Wu − *State Key Laboratory of Chem/Bio-Sensing and Chemometrics, College of Chemistry and Chemical*

Engineering, Hunan University, Changsha 410082 Hunan, China

Yanhong Lyu − *State Key Laboratory of Chem/Bio-Sensing and Chemometrics, College of Chemistry and Chemical Engineering, Hunan University, Changsha 410082 Hunan, China; School of Physics and Chemistry, Hunan First Normal University, Changsha 410205 Hunan, China*

Wei Chen − *State Key Laboratory of Chem/Bio-Sensing and Chemometrics, College of Chemistry and Chemical Engineering, Hunan University, Changsha 410082 Hunan, China*

Huaijuan Zhou − *Advanced Research Institute of Multidisciplinary Sciences, Beijing Institute of Technology, Beijing 100081, China*

Roland De Marco − *Department of Chemistry, School of Pure Science, College of Engineering, Science and Technology, Fiji National University, Suva 15676, Fiji; School of Chemistry and Molecular Biosciences, The University of Queensland, Brisbane, Queensland 4072, Australia;* ⊙ orcid.org/0000-0002-1357-3727

Nataliya Tsud − *Faculty of Mathematics and Physics, Department of Surface and Plasma Science, Charles University, Prague 18000, Czech Republic;* ⊙ orcid.org/0000-0001-7439-7731

Kevin C. Prince − *Elettra-Sincrotrone Trieste S.c.p.A., Trieste 34149, Italy;* ⊙ orcid.org/0000-0002-5416-7354

Viacheslav Kalinovych − *Faculty of Mathematics and Physics, Department of Surface and Plasma Science, Charles University, Prague 18000, Czech Republic*

Bernt Johannessen − *Australian Synchrotron, Clayton, Victoria 3168, Australia*

San Ping Jiang − *WA School of Mines: Minerals, Energy and Chemical Engineering, Curtin University, Perth, Western Australia 6102, Australia;* ⊙ orcid.org/0000-0002-7042-2976

Shuangyin Wang − *State Key Laboratory of Chem/Bio-Sensing and Chemometrics, College of Chemistry and Chemical Engineering, Hunan University, Changsha 410082 Hunan, China*

Complete contact information is available at:
https://pubs.acs.org/10.1021/jacsau.2c00690

Author Contributions

B.W., Y.L., and W.C. contributed equally. J.Z. conceived the ideas, designed the research, and oversaw the entire project. B.W., Y.L., and W.C. synthesized and characterized the catalysts, conducted PEC measurements, and analyzed the data. H.Z., R.D.M., N.T., K.C.P., V.K., and J.Z. implemented the XPS measurements and analyzed these data. B.J. applied and completed the XAS measurements and assisted J.Z. with the analysis of data. J.Z., Y.L., R.D.M., N.T., K.C.P., B.J., S.P.J., and S.W. co-wrote the paper and/or provided intellectual input to the manuscript. All authors have given approval to the final version of the manuscript. CRediT: **Binbin Wu** methodology, writing-original draft; **Yanhong Lyu** funding acquisition, methodology; **Wei Chen** methodology; **Jianyun Zheng** conceptualization, funding acquisition, supervision, writing-original draft, writing-review & editing; **Huaijuan Zhou** methodology; **Roland De Marco** methodology, resources; **Nataliya Tsud** methodology; **Kevin Charles Prince** methodology; **Viacheslav Kalinovych** methodology; **Bernt Johannessen** methodology; **San Ping Jiang** methodology, writing-

■ REFERENCES

(1) Morton, O. A new day dawning?: Silicon Valley sunrise. *Nature* **2006**, *443*, 19−22.

(2) Wang, Z.; Li, C.; Domen, K. Recent developments in heterogeneous photocatalysts for solar-driven overall water splitting. *Chem. Soc. Rev.* **2019**, *48*, 2109−2125.

(3) Yoshikawa, K.; Kawasaki, H.; Yoshida, W.; Irie, T.; Konishi, K.; Nakano, K.; Uto, T.; Adachi, D.; Kanematsu, M.; Uzu, H.; Yamamoto, K. Silicon heterojunction solar cell with interdigitated back contacts for a photoconversion efficiency over 26. *Nat. Energy* **2017**, *2*, 17032.

(4) Fujishima, A.; Honda, K. Electrochemical Photolysis of Water at a Semiconductor Electrode. *Nature* **1972**, *238*, 37−38.

(5) Lewis, N. S. Research opportunities to advance solar energy utilization. *Science* **2016**, *351*, aad1920.

(6) Andrei, V.; Jagt, R. A.; Rahaman, M.; Lari, L.; Lazarov, V. K.; MacManus-Driscoll, J. L.; Hoye, R. L. Z.; Reisner, E. Long-Term Solar Water and CO_2 Splitting with Photoelectrochemical BiOI-$BiVO_4$ Tandems. *Nat. Mater.* **2022**, *21*, 864−868.

(7) Andrei, V.; Ucoski, G. M.; Pornrungroj, C.; Uswachoke, C.; Wang, Q.; Achilleos, D. S.; Kasap, H.; Sokol, K. P.; Jagt, R. A.; Lu, H.; Lawson, T.; Wagner, A.; Pike, S. D.; Wright, D. S.; Hoye, R. L. Z.; MacManus-Driscoll, J. L.; Joyce, H. J.; Friend, R. H.; Reisner, E. Floating Perovskite-$BiVO_4$ Devices for Scalable Solar Fuel Production. *Nature* **2022**, *608*, 518−522.

(8) Chen, X.; Shen, S.; Guo, L.; Mao, S. S. Semiconductor-Based Photocatalytic Hydrogen Generation. *Chem. Rev.* **2010**, *110*, 6503−6570.

(9) Sivula, K.; van de Krol, R. Semiconducting materials for photoelectrochemical energy conversion. *Nat. Rev. Mater.* **2016**, *1*, 15010.

(10) Xiao, M.; Wang, Z.; Lyu, M.; Luo, B.; Wang, S.; Liu, G.; Cheng, H. M.; Wang, L. Hollow nanostructures for photocatalysis: Advantages and challenges. *Adv. Mater.* **2019**, *31*, 1801369.

(11) Yu, X.; Marks, T. J.; Facchetti, A. Metal oxides for optoelectronic applications. *Nat. Mater.* **2016**, *15*, 383−396.

(12) Linic, S.; Christopher, P.; Ingram, D. B. Plasmonic-metal nanostructures for efficient conversion of solar to chemical energy. *Nat. Mater.* **2011**, *10*, 911−921.

(13) Cowan, A. J.; Durrant, J. R. Long-lived charge separated states in nanostructured semiconductor photoelectrodes for the production of solar fuels. *Chem. Soc. Rev.* **2013**, *42*, 2281−2293.

(14) Baldini, E.; Dominguez, A.; Palmieri, T.; Cannelli, O.; Rubio, A.; Ruello, P.; Chergui, M. Exciton control in a room temperature bulk semiconductor with coherent strain pulses. *Sci. Adv.* **2019**, *5*, No. eaax2937.

(15) Chen, C.; Avila, J.; Frantzeskakis, E.; Levy, A.; Asensio, M. C. Observation of a two-dimensional liquid of Fröhlich polarons at the bare $SrTiO_3$ surface. *Nat. Commun.* **2015**, *6*, 8585.

(16) Emin, D.; Seager, C. H.; Quinn, R. K. Small-Polaron Hopping Motion in Some Chalcogenide Glasses. *Phys. Rev. Lett.* **1972**, *28*, 813−816.

(17) Selim, S.; Pastor, E.; García-Tecedor, M.; Morris, M. R.; Francàs, L.; Sachs, M.; Moss, B.; Corby, S.; Mesa, C. A.; Gimenez, S.; Kafizas, A.; Bakulin, A. A.; Durrant, J. R. Impact of Oxygen Vacancy Occupancy on Charge Carrier Dynamics in $BiVO_4$ Photoanodes. *J. Am. Chem. Soc.* **2019**, *141*, 18791−18798.

(18) Zheng, J.; Zhou, H.; Zou, Y.; Wang, R.; Lyu, Y.; Jiang, S. P.; Wang, S. Efficiency and stability of narrow-gap semiconductor-based photoelectrodes. *Energy Environ. Sci.* **2019**, *12*, 2345−2374.

(19) Mesa, C. A.; Francàs, L.; Yang, K. R.; Garrido-Barros, P.; Pastor, E.; Ma, Y.; Kafizas, A.; Rosser, T. E.; Mayer, M. T.; Reisner, E.; Grätzel, M.; Batista, V. S.; Durrant, J. R. Multihole water oxidation catalysis on haematite photoanodes revealed by operando spectroelectrochemistry and DFT. *Nat. Chem.* **2020**, *12*, 82−89.

(20) Verlage, E.; Hu, S.; Liu, R.; Jones, R. J. R.; Sun, K.; Xiang, C.; Lewis, N. S.; Atwater, H. A. A monolithically integrated, intrinsically safe, 10% efficient, solar-driven water-splitting system based on active, stable earth-abundant electrocatalysts in conjunction with tandem III−V light absorbers protected by amorphous TiO_2 films. *Energy Environ. Sci.* **2015**, *8*, 3166−3172.

(21) Corby, S.; Francàs, L.; Selim, S.; Sachs, M.; Blackman, C.; Kafizas, A.; Durrant, J. R. Water Oxidation and Electron Extraction Kinetics in Nanostructured Tungsten Trioxide Photoanodes. *J. Am. Chem. Soc.* **2018**, *140*, 16168−16177.

(22) Pan, L.; Kim, J. H.; Mayer, M. T.; Son, M. K.; Ummadisingu, A.; Lee, J. S.; Hagfeldt, A.; Luo, J.; Grätzel, M. Boosting the performance of Cu_2O photocathodes for unassisted solar water splitting devices. *Nat. Catal.* **2018**, *1*, 412−420.

(23) White, J. S.; Bator, M.; Hu, Y.; Luetkens, H.; Stahn, J.; Capelli, S.; Das, S.; Döbeli, M.; Lippert, T.; Malik, V. K.; Martynczuk, J.; Wokaun, A.; Kenzelmann, M.; Niedermayer, C.; Schneider, C. W. Strain-Induced Ferromagnetism in Antiferromagnetic $LuMnO_3$ Thin Films. *Phys. Rev. Lett.* **2013**, *111*, 037201.

(24) Zheng, J. Y.; Bao, S. H.; Lv, Y. H.; Jin, P. Activation and enhancement of room-temperature ferromagnetism in Cu-doped anatase TiO_2 films by bound magnetic polaron and oxygen defects. *ACS Appl. Mater. Interfaces* **2014**, *6*, 22243−22249.

(25) Zheng, J. Y.; Bao, S. H.; Guo, Y.; Jin, P. Natural hydrophobicity and reversible wettability conversion of flat anatase TiO_2 thin film. *ACS Appl. Mater. Interfaces* **2014**, *6*, 1351−1355.

(26) Roose, B.; Pathak, S.; Steiner, U. Doping of TiO_2 for sensitized solar cells. *Chem. Soc. Rev.* **2015**, *44*, 8326−8349.

(27) Schneider, J.; Matsuoka, M.; Takeuchi, M.; Zhang, J.; Horiuchi, Y.; Anpo, M.; Bahnemann, D. W. Understanding TiO_2 Photocatalysis: Mechanisms and Materials. *Chem. Rev.* **2014**, *114*, 9919−9986.

(28) Liu, M.; Johnston, M. B.; Snaith, H. J. Efficient planar heterojunction perovskite solar cells by vapour deposition. *Nature* **2013**, *501*, 395−398.

(29) Zheng, J.; Lyu, Y.; Wang, R.; Xie, C.; Zhou, H.; Jiang, S. P.; Wang, S. Crystalline TiO_2 protective layer with graded oxygen defects for efficient and stable silicon-based photocathode. *Nat. Commun.* **2018**, *9*, 3572.

(30) Zhou, G.; Wang, P.; Li, H.; Hu, B.; Sun, Y.; Huang, R.; Liu, L. Spin-sate reconfiguration induced by alternating magnetic field for efficient oxygen evolution reaction. *Nat. Commun.* **2021**, *12*, 4827.

(31) Zheng, J.; Lyu, Y.; Xie, C.; Wang, R.; Tao, L.; Wu, H.; Zhou, H.; Jiang, S.; Wang, S. Defect-Enhanced Charge Separation and Transfer within Protection Layer/Semiconductor Structure of Photoanodes. *Adv. Mater.* **2018**, *30*, No. e1801773.

(32) Yu, Y.; Zhang, Z.; Yin, X.; Kvit, A.; Liao, Q.; Kang, Z.; Yan, X.; Zhang, Y.; Wang, X. Enhanced photoelectrochemical efficiency and

stability using a conformal TiO$_2$ film on a black silicon photoanode. *Nat. Energy* **2017**, *2*, 17045.

(33) Zheng, J.; Lyu, Y.; Qiao, M.; Veder, J. P.; Marco, R. D.; Bradley, J.; Wang, R.; Li, Y.; Huang, A.; Jiang, S. P.; Wang, S. Tuning the Electron Localization of Gold Enables the Control of Nitrogen-to-Ammonia Fixation. *Angew. Chem.* **2019**, *58*, 18604−18609.

(34) van der Laan, G. Polaronic satellites in x-ray-absorption spectra. *Phys. Rev. B* **1990**, *41*, 12366−12368.

(35) Idriss, H.; Pierce, K. G.; Barteau, M. A. Synthesis of Stilbene from Benzaldehyde by Reductive Coupling on TiO$_2$(001) Surfaces. *J. Am. Chem. Soc.* **1994**, *116*, 3063−3074.

(36) Pan, J.; Liu, G.; Lu, G. Q.; Cheng, H. M. On the True Photoreactivity Order of {001}, {010}, and {101} Facets of Anatase TiO$_2$ Crystals. *Angew. Chem., Int. Ed.* **2011**, *50*, 2133−2137.

(37) Souza-Neto, N. M.; Haskel, D.; Tseng, Y. C.; Lapertot, G. Pressure-Induced Electronic Mixing and Enhancement of Ferromagnetic Ordering in Eu X (X=Te, Se, S, O) Magnetic Semiconductors. *Phys. Rev. Lett.* **2009**, *102*, 057206.